Application and Extension of the Particle X-ray Coincidence Technique to Astrophysical Reaction Rates

L. J. Sun[a], J. Dopfer[b,a], A. Adams[b,a], C. Wrede[b,a,*], A. Banerjee[c], B. A. Brown[b,a], R. Mahajan[a], T. Rauscher[d,e], C. Sumithrarachchi[a], D. Weisshaar[a], T. Wheeler[b,a]

[a]*Facility for Rare Isotope Beams, Michigan State University, East Lansing, Michigan 48824, United States*
[b]*Department of Physics and Astronomy, Michigan State University, East Lansing, Michigan 48824, United States*
[c]*Saha Institute of Nuclear Physics, 1/AF, Bidhan Nagar, Kolkata 700064, India*
[d]*Department of Physics, University of Basel, 4056 Basel, Switzerland*
[e]*Centre for Astrophysics Research, University of Hertfordshire, Hatfield AL10 9AB, United Kingdom*

Abstract

Lifetimes of excited nuclear states are critical for understanding nuclear structure and astrophysical modeling. It has been demonstrated that the particle-X-ray coincidence technique (PXCT) developed based on an atomic clock technique can provide one of the most effective ways to probe the lifetimes of excited nuclear states in the time range of 10^{-17} – 10^{-15} s. We have developed a detection system at the Facilities for Rare Isotope Beams to extend this technique to measure the lifetimes of discrete resonances essential for thermonuclear reaction rate calculations. The performance of the PXCT system has been thoroughly tested using radioactive sources. This setup is ready for ^{60}Ga decay measurement with full-power FRIB, paving the way for a strong constraint on the strength of the NiCu cycle in the rapid proton capture process.

1. Introduction

In the 1970s, the Particle X-ray Coincidence Technique (PXCT) was initially demonstrated and applied to measure the average lifetimes of proton-unbound states in ^{69}As populated by the electron capture (EC) of ^{69}Se [1]. The principle of the method is illustrated in Fig. 1. In the process of an EC-delayed proton emission, a proton-rich precursor with an atomic number of Z decays by K-EC to the proton emitter $(Z-1)$. Due to the EC, a proton unbound nuclear state and an atomic shell vacancy are created simultaneously. An atomic electron in a higher-lying shell fills the vacancy with typical lifetimes of $\tau_{K\text{shell}} = 0.01$ to 1.0 fs and emits the characteristic X ray. Meanwhile, the proton-unbound state with a comparable lifetime $\tau_{p-\text{emit}}$ emits a proton to a state of the daughter $(Z-2)$. If the proton is emitted before the X-ray emission, then the characteristic X-ray energy will correspond to the atomic number of the daughter $(Z-2)$. If the proton is emitted after the X-ray emission, then the X-ray energy will be characteristic of the atomic number of the proton emitter $(Z-1)$. By measuring the spectrum of X rays in coincidence with protons and counting the relative intensities of the $Z-1$ and $Z-2$ X-ray peaks $I_{KX(Z-1)}/I_{KX(Z-2)}$, the lifetimes of proton-emitting states can be related to the lifetimes of the emitter K-shell vacancies by the relation

$$\frac{\tau_{p-\text{emit}}}{\tau_{K\text{shell}}} = \frac{\Gamma_{K\text{shell}}}{\Gamma_{p-\text{emit}}} = \frac{I_{KX(Z-1)}}{I_{KX(Z-2)}}, \quad (1)$$

where the decay width $\Gamma_{K\text{shell}}$ and $\Gamma_{p-\text{emit}}$ is the equivalent of $\hbar/\tau_{K\text{shell}}$ and $\hbar/\tau_{p-\text{emit}}$, respectively, as they both follow the exponential decay law. Because the K-shell vacancy lifetimes are well known both experimentally and theoretically, ranging from $\tau \approx 2\times10^{-15}$ s for carbon down to $\tau \approx 6\times10^{-18}$ s for uranium [2, 3], lifetimes of proton-emitting states can be established with reasonable accuracy. The preceding discussion is also generalizable to EC-delayed α-particle emission. This 'atomic clock' method has been successfully applied to measure the average sub-fs lifetimes of proton-unbound states populated by the ECs of ^{65}Ge [4], ^{69}Se [4, 5], ^{73}Kr [4, 6, 7], ^{77}Sr [4], ^{113}Xe [8], and ^{117}Ba [9].

In all the aforementioned cases, excited states could not be distinguished individually as their level density was too high, and none of the measured lifetimes were discussed in an astrophysical context. High-resolution measurements on γ rays and protons would enable refinement of the PXCT by introducing the possibility of selecting the initial proton-emitting state and the excited final state. We have buit a PXCT apparatus to extend this technique to constrain the lifetimes of resonances of interest for astrophysics.

2. Scientific Motivations

Type I X-ray bursts (XRBs) are the most frequent type of thermonuclear stellar explosions in the Galaxy. They are powered by thermonuclear runaways in hydrogen- and/or helium-rich material accreted onto the surface of a neutron star in a low-mass X-ray binary system. The main nuclear reaction flow in the XRB is driven toward the proton drip-line and to high masses via the αp-process (a sequence of (α, p) and (p, γ)

*Corresponding author
Email address: wrede@frib.msu.edu (C. Wrede)

reactions) and the rp-process (a series of rapid proton-captures and β^+-decays). Accurate nuclear physics inputs such as β decay rates, masses, and nuclear reaction rates of neutron-deficient rare isotopes along the path of the αp- and the rp-process are needed to model the energy production and nucleosynthesis in XRBs. Our understanding of XRBs has greatly expanded while they still hold many open questions despite decades of work [10, 11, 12].

In a recent investigation to identify important reaction rates that affect XRB observables and nucleosynthesis, the ^{59}Cu$(p,\gamma)^{60}$Zn and ^{59}Cu$(p,\alpha)^{56}$Ni reaction rates were predicted to have significant impacts on the modeling of X-ray burst light curves and the composition of the burst ashes [13]. Under XRB conditions, the reaction flux beyond ^{56}Ni is affected by several cycles. As indicated in Fig. 2, a low ^{59}Cu$(p,\gamma)^{60}$Zn or a high ^{59}Cu$(p,\alpha)^{56}$Ni rate leads to the formation of a stronger NiCu cycle that strongly limits the synthesis of heavier nuclei and also affects the shape of the observed light curves [14]. Proton-capture onto ^{59}Cu either returns the cycle to ^{56}Ni or breaks out via ^{59}Cu(p,γ), depending on the $(p,\gamma)/(p,\alpha)$ rate ratio. The critical quantity determining the strength of the NiCu cycle is the ratio of the (p,α) to (p,γ) reaction rates at ^{59}Cu.

For a narrow isolated resonance, the resonant reaction rate can be calculated using the well-known relation [15],

$$N_A\langle\sigma v\rangle_r = 1.5394\times10^{11}(\mu T_9)^{-3/2}\times\omega\gamma \times\exp\left(-\frac{11.605E_r}{T_9}\right)(\mathrm{cm^3s^{-1}mol^{-1}}), \quad (2)$$

where $\mu = A_T/(A_p + A_T)$ is the reduced mass in atomic mass units, with $A_p = 1$ and $A_T = 59$ as the mass numbers of proton and ^{59}Cu, respectively. E_r is the resonance energy in the center-of-mass system in units of MeV. T_9 is the temperature in units of giga kelvin (GK), and $\omega\gamma$ is the resonance strength in units of MeV, which is defined as:

$$\omega\gamma = \frac{2J_r+1}{(2J_p+1)(2J_T+1)}\frac{\Gamma_p\times\Gamma_\gamma}{\Gamma_{\rm tot}}, \quad (3)$$

where J_r is the spin of the resonance, $J_p = 1/2$ is the spin of proton, and $J_T = 3/2^-$ is the spin of the ground state of ^{59}Cu. The total decay width $\Gamma_{\rm tot}$ of the resonance is the sum of its partial decay widths, i.e., proton width (Γ_p), γ width (Γ_γ), and α width (Γ_α) since they represent the three open decay channels for the resonances of relevance to the thermonuclear ^{59}Cu$(p,\gamma)^{60}$Zn reaction rate. Alternatively, the resonance strength can be constructed by combining the level lifetime τ and the proton branching ratio $B_p = \Gamma_p/\Gamma_{\rm tot}$ using the following expression:

$$\omega\gamma = \frac{2J_r+1}{(2J_p+1)(2J_T+1)}B_pB_\gamma\frac{\hbar}{\tau}, \quad (4)$$

which are also applicable to the ^{59}Cu$(p,\alpha)^{56}$Ni reaction by replacing the γ terms with α terms ($J_\alpha = 0$). Therefore, measurements of the proton, γ-ray, and α-decay branching ratios, and the lifetimes of the ^{60}Zn resonances within the Gamow window will suffice to determine the contribution of resonant charged-particle capture to the total reaction rates. Usually, we could use two techniques, β decay spectroscopy and the Doppler-shift attenuation method, and therefore, two separate experiments to measure branching ratios and lifetimes and constrain thermonuclear rates. Applying the PXCT based on EC is well suited to measure both in a single experiment.

The Gamow energies and windows for the ^{59}Cu$(p,\gamma)^{60}$Zn and ^{59}Cu$(p,\alpha)^{56}$Ni reactions shown in Table 1 are calculated from a numerical study of the relevant energy ranges for astrophysical reaction rates [16]. It can be seen that at any given temperature below 2 GK, the corresponding effective energy windows will not exceed 2.8 MeV. Combined with the proton-separation energy of ^{60}Zn $S_p(^{60}\mathrm{Zn}) = 5105.0(4)$ keV and α-separation energy of ^{60}Zn $S_\alpha(^{60}\mathrm{Zn}) = 2691.7(5)$ keV, the excitation energy of interest should be from 5.1 to 7.9 MeV. Therefore, the key resonances in ^{60}Zn are energetically accessible in the β decay of ^{60}Ga owing to the large $Q_{\rm EC}(^{60}\mathrm{Ga}) = 14161(13)$ keV. In a recent ^{58}Ni$(^3\mathrm{He},n)^{60}$Zn reaction measurement [17], the nuclear level density of ^{60}Zn was extracted from the neutron evaporation spectrum. For the excitation energies at 6 MeV, the level density is estimated to be only $\sim$18 MeV^{-1}. The β decay of the 2^+ ground state of ^{60}Ga preferentially populates $J^\pi = 1^+$, 2^+, and 3^+ states in ^{60}Zn according to the β-decay selection rules. As the $\ell = 1$ proton captures on the $3/2^-$ ^{59}Cu ground state populate ^{60}Zn 0^+, 1^+, 2^+, and 3^+ resonances, indicating an even lower level density for the states selected by β decay. All the ^{60}Zn states populated by allowed transitions are positive parity states, whereas the $\ell = 0, 2$ proton captures require a parity change. Based on our calculation, proton captures with $\ell = 0.2$ are less significant. It is expected to obtain the properties of the ^{60}Zn resonances by identifying the discrete states populated in the β-decay of ^{60}Ga (see Fig. 3).

To narrow down the important resonances, we performed shell-model calculations using the NuShellX@MSU code [25] in the full fp-shell model space with the GPFX1A interaction [26]. The properties of 72 ^{60}Zn states within excitation energies of 5 – 6.5 MeV are calculated and used as input to determine the resonant capture component of the ^{59}Cu$(p,\gamma)^{60}$Zn reaction rate. As shown in Table 2, the resonant capture contributions from four resonances are found to be dominant over a certain temperature range. A quenching factor $q^2 = 0.6$ for the matrix elements of the Gamow-Teller operator was used to calculate the β-feeding intensities in the ^{60}Ga decay. It can be seen that at least one of the four key resonances can be populated with a large decay branching ratio, and thus a lower limit on the ^{59}Cu$(p,\gamma)^{60}$Zn reaction rate would be set. A strong lower limit on the ^{59}Cu$(p,\gamma)^{60}$Zn reaction rate would indicate very weak NiCu cycling and therefore solve the astrophysical problem.

Even if the level density is still too high to distinguish discrete resonances, we can derive the particle and γ-transmission coefficients, which are essential ingredients to calculate the reaction rates with the statistical model [27]. Calculations in the statistical model require the input of a number of different statistical properties. The standard

Table 1: Gamow windows $\widetilde{E}_{\rm hi} - \widetilde{\Delta} \le E \le \widetilde{E}_{\rm hi}$ and Gamow peaks $\widetilde{E}_0$ for the ^{59}Cu$(p,\gamma)^{60}$Zn and ^{59}Cu$(p,\alpha)^{56}$Ni reactions at a temperature T.

	^{59}Cu$(p,\gamma)^{60}$Zn			^{59}Cu$(p,\alpha)^{56}$Ni		
T (GK)	$\widetilde{E}_{\rm hi} - \widetilde{\Delta}$ (MeV)	$\widetilde{E}_{\rm hi}$ (MeV)	$\widetilde{E}_0$ (MeV)	$\widetilde{E}_{\rm hi} - \widetilde{\Delta}$ (MeV)	$\widetilde{E}_{\rm hi}$ (MeV)	$\widetilde{E}_0$ (MeV)
0.5	0.51	0.92	0.71	0.55	0.98	0.74
1.0	0.67	1.26	0.91	0.73	1.48	1.01
1.5	0.75	1.57	1.01	0.87	2.11	1.27
2.0	0.82	1.83	1.14	1.01	2.80	1.74

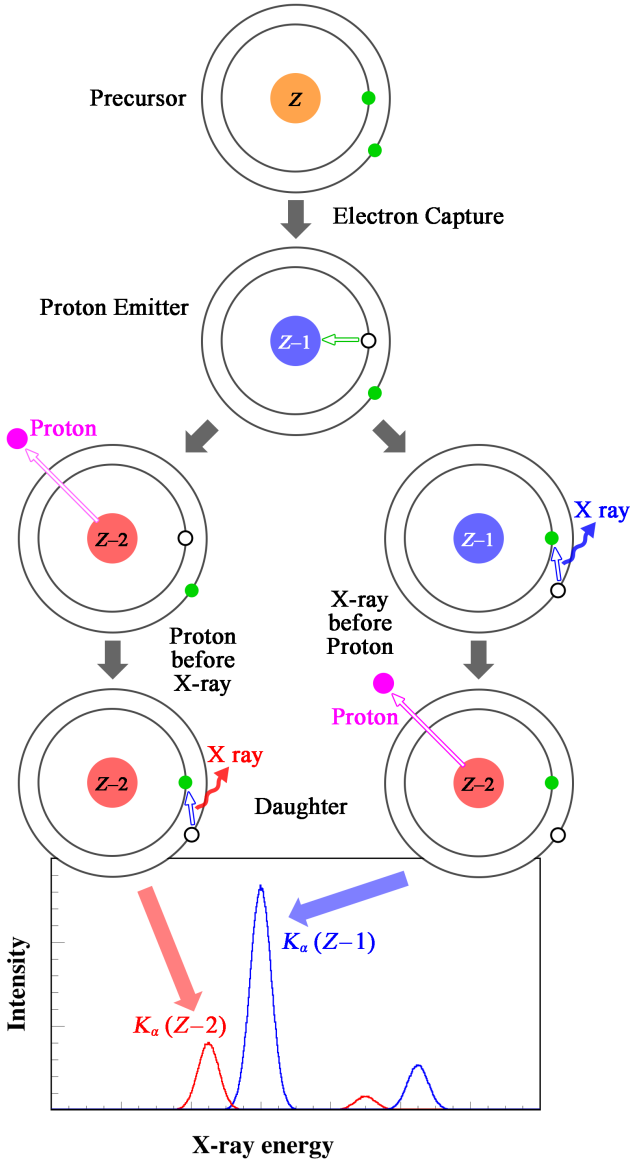

Figure 1: Cartoon illustrating the proton-X-ray coincidence technique. See text for details.

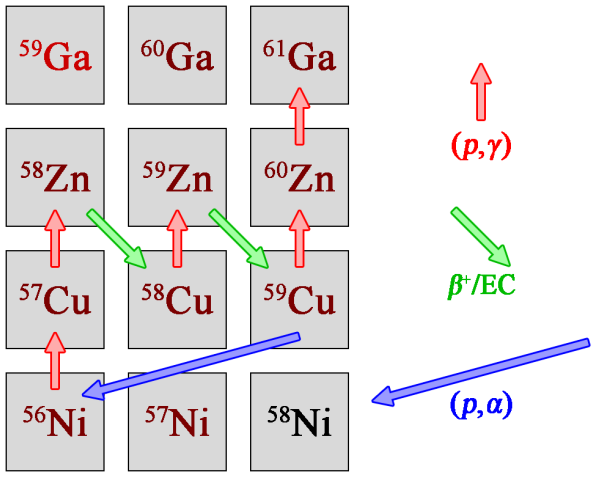

Figure 2: Portion of the *rp*-process reaction sequence featuring the NiCu reaction cycle.

Table 2: Properties of the dominant resonances in the ^{59}Cu$(p,\gamma)^{60}$Zn reaction from shell-model calculations. The values listed in the first through fifth columns are the dominating region of temperature, spin and parity (J^π), excitation energy (E^*), resonance energy (E_r), and β-feeding intensity (I_β) of each resonance, respectively.

T (GK)	J^π	E^* (keV)	E_r (keV)	I_β (%)
0.10 – 0.15	3^+	5362	257	0.05
0.15 – 0.45	1^+	5568	463	3.75
0.45 – 0.70	2^+	5648	543	0.15
0.70 – 7.50	2^+	6079	974	0.39

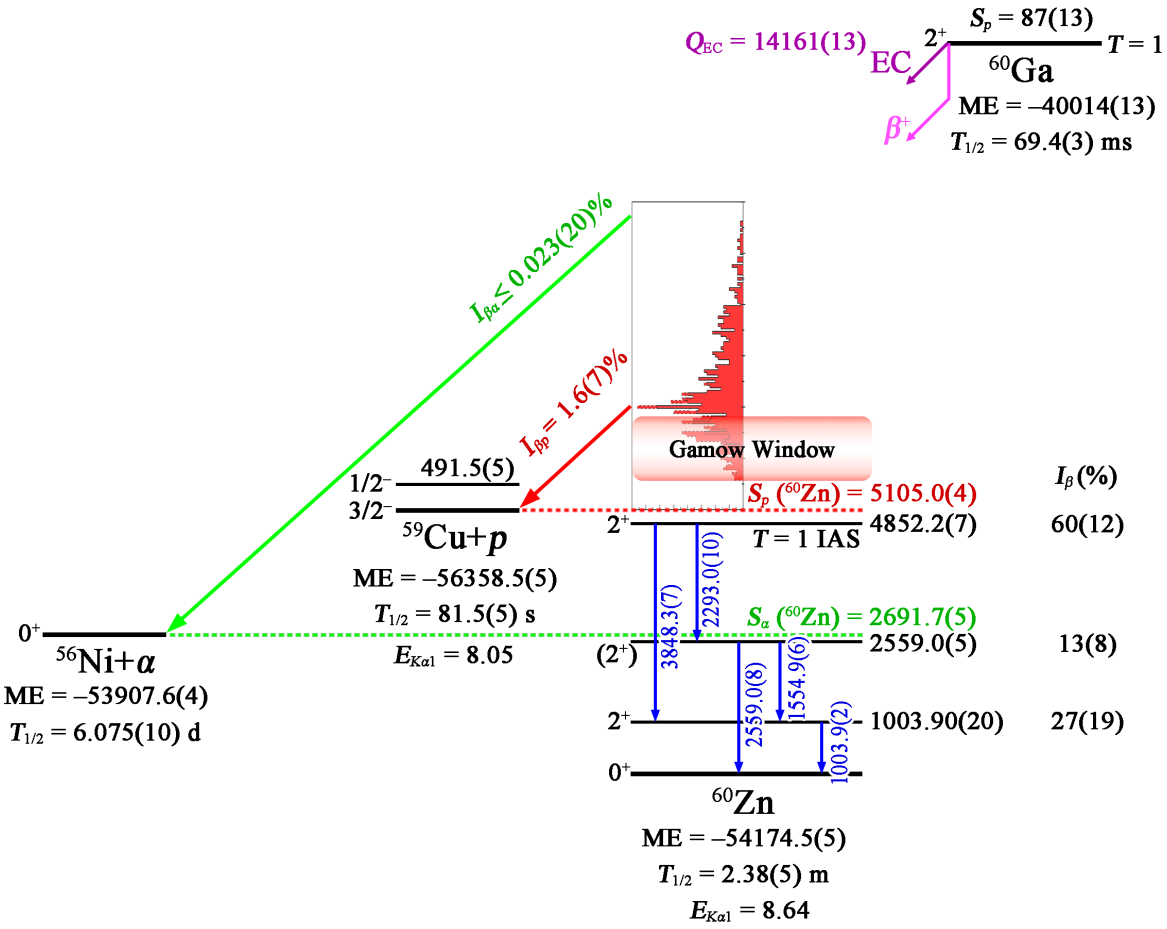

Figure 3: Previously established decay scheme of ^{60}Ga. All energies labeled in the scheme are given in units of keV. The mass excesses of ^{56}Ni, ^{59}Cu, and ^{60}Zn are from AME2020 [18]. The mass excess of ^{60}Ga is the weighted average of values reported by Refs. [19, 20]. The proton-separation energy and the β-decay Q-value of ^{60}Ga are obtained using this average mass. The spins, parities, and excitation energies are from the evaluation [21]. The γ-ray energies, β-feeding intensities, and the proton spectrum are from ^{60}Ga β spectroscopy of [22]. The half-life of ^{60}Ga is the weighted average of values reported by Refs. [19, 22, 23, 24].

approach in the calculation of reaction rates for astrophysics in a Hauser-Feshbach statistical model is to include a number of discrete excited states when experimentally known. The important ingredients of statistical model calculations are the particle and γ-transmission coefficients T and the level density of excited states ρ [28]. Currently, experimental information on the ^{59}Cu$(p,\gamma)^{60}$Zn and ^{59}Cu$(p,\alpha)^{56}$Ni reactions is scarce. A direct cross-section measurement of the ^{59}Cu$(p,\alpha)^{56}$Ni reaction at energies far higher than the Gamow window for X-ray bursts was found to be lower than statistical model calculations [29]. The PXCT approach has wide applicability to constrain other reaction rates of particular importance in the rp-process. As ^{64}Ge plays an analogous role in the ZnGa cycle to the role of ^{60}Zn in the NiCu cycle, it is desirable to extend this method to study the β-decay of ^{64}As in the future.

In addition to the lifetimes obtained from the measured K X-ray intensities, the system also measures proton, γ-ray, and α-particle branching ratios (Γ_p/Γ, Γ_γ/Γ, Γ_α/Γ), ideally for discrete resonances for the first time. By gating on different protons and γ rays, we can extract the lifetime for a specific state. This method will also provide experimental information on the nuclear level density and transmission coefficients needed to calculate rates using the statistical model.

3. Experimental Setup

3.1. Beam delivery

The Facility for Rare Isotope Beams (FRIB) full-power linear accelerator [30] will accelerate ^{70}Ge to 256 MeV/u with a beam power up to 400 kW. The reaction products from ^{70}Ge impinging on a rotating carbon target will be separated by the Advanced Rare Isotope Separator [31]. A cocktail fast beam containing ^{60}Ga and some nearby isotones will be slowed down in metal degraders with momentum compression and thermalized in gas stoppers filled with helium [32, 33]. The thermalized ^{60}Ga ions will drift towards a nozzle and exit into a radio-frequency quadrupole ion-guide system. The ions will be guided and accelerated to 30 keV through a combination of radio-frequency and direct-current fields before being delivered to the stopped beam area [34]. The intensity of the ^{60}Ga stopped beam is optimistically estimated to be 9.2×10^3 pps.

As shown in Fig. 4, we have built a PXCT detection system that will be used in the stopped beam area. The beam will be tuned into our vacuum chamber and implanted into an Aluminized Mylar foil tilted at a 45° angle with respect to the beam direction. Thermalized beams can be fully stopped by a thin collection foil, thereby reducing the attenuation of photons and charged particles as compared to using fast beams. The detection system comprises a silicon detector telescope for charged-particle detection via energy-loss and residual energy (ΔE-E), two large-volume coaxial germanium detectors for γ-ray detection, and a planar germanium detector for X-ray detection. The flexible design allows for the versatile combination of individual detectors for various experimental purposes.

3.2. Detectors

We have selected two single-sided single-area circular Si detectors, MSD12 of 12 μm thickness [35] and MSD26 of 1000 μm thickness [36] manufactured by Micron Semiconductor Ltd to construct the ΔE-E telescope. The numbers following MSD indicate the active area diameter in millimeters. The dead layer window and metallization type for MSD12 are 9.5P/7P, and for MSD26 are 9.5P/2M. Here, 9.5 represents a boron-doped silicon dead layer with a thickness of 50 nm, 7 represents a dead layer with a thickness of 300 nm, and 2 represents a dead layer with a thickness of 500 nm. P denotes a periphery metal band with a width of 30 μm around the edge of the active areas and contact pads for wire bonding. The majority of the active area does not have metal coverage. M denotes a continuous aluminum coverage with a thickness of 300 nm over the entire active area region. Both silicon chips are assembled onto an FR4-printed circuit board. MSD26 is positioned 4.4 mm behind MSD12. MSD12 is 11.7 mm from the target center and defines the solid angle coverage of the telescope at 5.5% of 4π.

We have selected a Low Energy Germanium detector (LEGe), Mirion GL0510, for X-ray detection [37]. The LEGe detector consists of a Ge crystal with a diameter of 25.0 mm and a length of 10.5 mm. LEGe is housed in a cryostat with a diameter of 38.1 mm and a 0.13-mm thick beryllium entrance window 10.5 mm from the center of the vacuum chamber, ideally suited for X-ray spectroscopy from 3 keV up. The Ge crystal is positioned 5.6 mm from the entrance window, covering 10.5% of the 4π solid angle. LEGe is fabricated with a thin p^+ contact on the front and side and a rear n^+ contact that covers less than the full area, resulting in lower capacitance than a similar-sized planar device. Since preamplifier noise is a function of detector capacitance, LEGe features low noise and high resolution at low and moderate energies.

We have selected two Extended Range Coaxial Germanium Detectors (XtRa), Mirion GX10020, for γ-ray detection [38]. The active volume of XtRa1 has a diameter of 84.8 mm and a thickness of 65.2 mm, while XtRa2 has a diameter of 79.8 mm and a thickness of 80.0 mm. Conventional coaxial detectors have a lithium-diffused n^+ contact typically of 0.5 to 1.5 mm thickness on the outer surface, which forms a dead layer that stops most photons below 40 keV, rendering the detector inefficient at low energies. However, the XtRa detectors feature an exclusive thin window contact on the front surface and a n^+ contact on the side. The cryostat window is made of a 0.6-mm-thick carbon composite, enabling a good low-energy response.

All three Ge detectors are equipped with the Cryo-Pulse 5 Plus (CP5-Plus) electrically refrigerated cryostat. A 5-watt pulse tube cooler is integrated into a compact coldhead assembly, which is directly attached to the detector housing. CP5-Plus features low vibration, low noise, low power demand, and a maintenance-free operation, with an estimated Mean Time Between Failures of 3,000,000 hours [39]. The assembly is connected to a bench-top power controller that

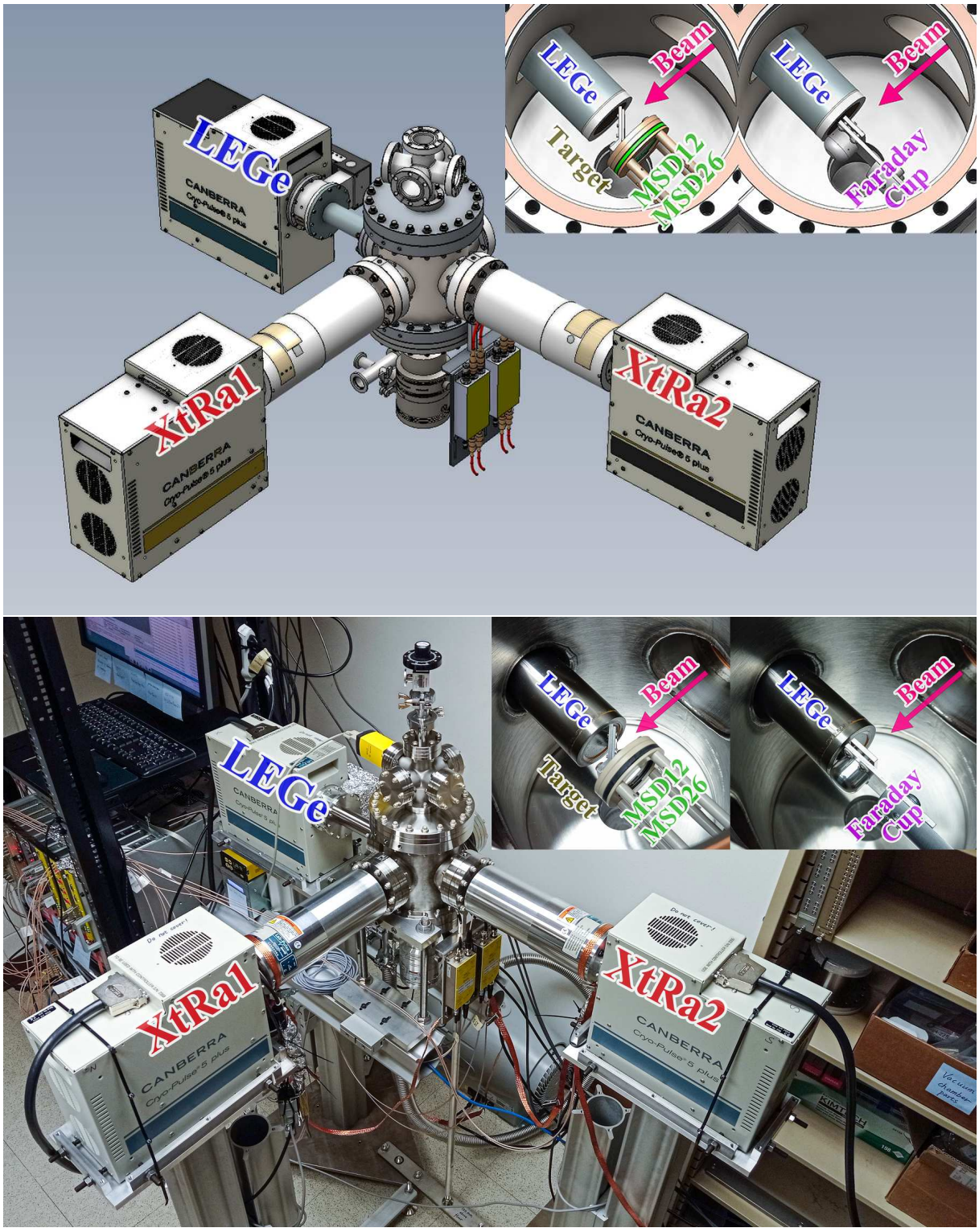

Figure 4: Mechanical design drawing and photograph of the PXCT detection system. The insets highlight two configurations: a Faraday cup with a collimator for beam tuning or a target foil and Si detectors for measurements.

provides the required output voltage to drive the compressor. The controller also contains the necessary logic to ensure the safe and reliable operation of the cryostat. An RS-232 serial interface and CP5-Plus control panel application are also included, allowing for remote monitoring of the cooler status.

3.3. Electronics

The Ge is connected to the Intelligent Preamplifier (iPA) [40], which incorporates a low-noise field-effect transistor (FET) input circuit optimized for the ultra-high source impedance of germanium detectors. The input circuits are cooled by mounting them inside the cryostat. The first stage of iPA serves as an integrator, providing an output voltage proportional to the accumulated charge from the detector, and also functions as an electrometer for measuring the leakage current of the detector. The second stage acts as an output buffer and allows for four conversion factors of 50, 100, 250, and 500 mV/MeV. The iPA generates an inverted output signal that is split into two outputs, each with a termination impedance of 93 and 50 Ω. A USB interface and a control panel application provide real-time monitoring of detector current, temperatures, and preamplifier operating voltages. The four output gains, as well as external or internal test pulsers, are selectable via the control panel application. iPA is equipped with a warm-up sensor that is thermally connected to the detector. The coldhead is also equipped with temperature sensors. In the event that the temperature exceeds the normal operating range, these sensors trigger the high-voltage inhibit signal from the preamplifier and the controller, respectively, providing protection to the Ge detectors.

Two ORTEC 660 Dual Bias Supply modules [41] are used to provide bias voltages to the three Ge detectors. We apply a negative bias to the p^+ contacts of LEGe and a positive bias to the n^+ contacts of XtRa. LEGe becomes fully depleted at −600 V and is recommended to be operated at −1100 V. XtRa1 and XtRa2 become fully depleted at a bias voltage of +4000 V and +2200 V, respectively, and both operate at +4500 V. ORTEC 660 includes a remote bias shutdown feature to protect the preamplifier FET against damage in the instance of accidental warm-up of the Ge detector. The typical leakage currents of the two XtRa detectors are below 20 pA and below 100 pA for LEGe. A Mesytec MHV 4-channel bias supply module with remote control features provides the bias voltages to the two MSD Si detectors. MSD12 has a depletion voltage of 1.5 V and is operated at 3.0 V, and MSD26 has a 90-V depletion voltage and is operated at 130 V. We apply a negative bias to the p^+ contacts of both MSD detectors through MPR-1 charge-sensitive preamplifiers [42] and the n^+ contacts are grounded. MHV offers a ramp speed as low as 5 V/s to protect the circuits of preamplifiers [43]. MSD26 has a leakage current of approximately 60 nA, whereas MSD12 maintains a leakage current below 1 nA. All the preamplifiers are powered by two Mesytec MNV-4 NIM power distribution and control modules [44].

Table 3: DDAS trapezoidal filter parameter settings for each detector.

Parameter	LEGe	XtRa1	XtRa2	MSD12	MSD26
Energy T_{Rise} (μs)	7.168	10.240	10.752	9.984	2.048
Energy T_{Gap} (μs)	0.768	1.792	1.280	2.944	1.024
Trigger T_{Rise} (μs)	0.200	0.200	0.200	0.112	0.248
Trigger T_{Gap} (μs)	0.104	0.104	0.104	0.304	0.200
CFD Delay (μs)	0.304	0.200	0.200	0.304	0.304
Tau (μs)	50	50	50	120	120

3.4. Data Acquisition System

All the preamplifier signals are transmitted via double-shielded RG316 coaxial cables of equal length and then digitized by a 16-bit, 250 MHz Pixie-16 module manufactured by XIA LLC [45]. The input impedance of each channel in Pixie-16 is configured to be 1 kΩ. A general-purpose nuclear physics data acquisition system Digital Data Acquisition System (DDAS) is used [46, 47] for recording and processing data. Trapezoidal filtering algorithms are implemented in both the slow filter for pulse amplitude measurement and the fast filter for leading-edge triggering. Each event is timestamped using a Constant Fraction Discriminator (CFD) algorithm based on the trigger filter response. The system operates in an internally triggered mode: recording data on a channel-by-channel basis whenever the trigger filter crosses the user-defined threshold. The data from all channels is ordered in time and subsequently assembled into events based on a user-defined event window length. The event timestamp is counted with 125 MHz clock ticks, i.e., 8 ns intervals.

The tail pulses from MPR-1 exhibit rise times of 400 ns (MSD12) and 70 ns (MSD26), with a 120 μs decay constant. The tail pulses from iPA exhibit rise times of 150 ns (LEGe) and 250 ns (XtRa), with a 50 μs decay constant. The DDAS filter parameters (Table 3) are optimized based on these observations [47, 48, 49]. The pulse amplitude is extracted from the energy filter amplitude at approximately $T_{\mathrm{Rise}} + T_{\mathrm{Gap}}$ after triggering. If a second trigger arrives within $T_{\mathrm{Rise}} + T_{\mathrm{Gap}}$, a pileup will occur. The energy filter parameters are the dominant factor in determining the count rate capacity of the DDAS system. A DB-2 Random Pulser [50] is used to investigate the data acquisition dead time. The time intervals between successive pulses obey a Poisson distribution function. Under the conditions specified in Table 3, the count rate performance is shown in Fig. 5. The observed event losses are in line with pile-up rates defined by the energy filter settings [46].

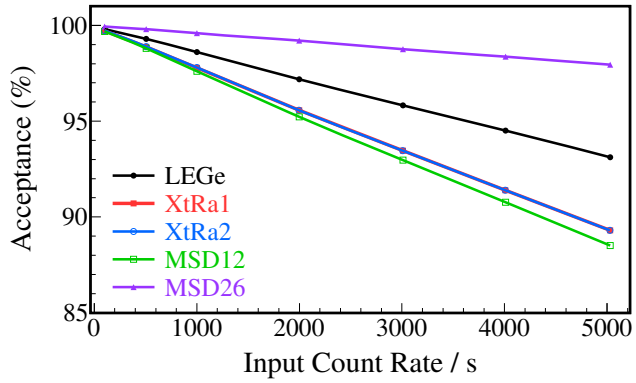

Figure 5: DDAS count rate performance.

4. Performance Tests

We have performed comprehensive tests on the PXCT system using the configuration illustrated in Fig. 6.

4.1. X-ray measurements

We have evaluated the performance of LEGe using the X rays and low-energy γ rays from ^{55}Fe, ^{152}Eu, and ^{241}Am radioactive sources, as shown in Fig. 7. The overall energy resolution achieved by LEGe is characterized by fitting the well-known X-ray or γ-ray lines with an exponentially modified Gaussian (EMG) function to account for incomplete charge collection [51, 52] at 5.90 keV (Mn $K_{\alpha1}$), 6.49 keV (Mn $K_{\beta1}$), 11.89 keV (Np L_{ℓ}), 13.76 keV (Np $L_{\alpha2}$), 13.95 keV (Np $L_{\alpha1}$), 26.34 keV (^{237}Np γ), 33.20 keV (^{237}Np γ), 39.52 keV (Sm $K_{\alpha2}$), 40.12 keV (Sm $K_{\alpha1}$), 45.29 keV (Sm $K_{\beta3}$), 45.41 keV (Sm $K_{\beta1}$), and 59.54 keV (^{237}Np γ). At the energies of interest, 8.05 keV (Cu $K_{\alpha1}$) and 8.64 keV (Zn $K_{\alpha1}$), the full width at half maximum is estimated to be 238(8) and 241(7) eV, respectively, providing enough resolving power to distinguish between the characteristic X rays of the proton emitter Zn and the daughter Cu.

For photons below 100 keV interacting with Ge, the photoelectric effect is predominant, i.e., the photon is absorbed, and its energy is transferred to an electron and causes prompt emission of a characteristic X ray as the resulting vacancy in the electron shell is filled. A full-energy peak is still observed if this X ray is reabsorbed near the original interaction site. However, if the photoelectric interaction occurs near the surface of Ge, the X ray is more likely to escape, which results in peaks usually at 9.89 keV and 10.98 keV below the photopeaks, known as the Ge escape peaks (Fig. 7). These energy differences correspond to the characteristic $K_{\alpha1}$ and $K_{\beta1}$ X-ray energies for Ge, respectively [53].

For photon energies just above the K-shell binding energy of Ge, 11103.0 ± 2.0 eV [53], the incident photon is strongly absorbed without deep penetration beyond the detector surface. The subsequent characteristic K X ray tends to escape, thereby decreasing the full energy peak efficiency.

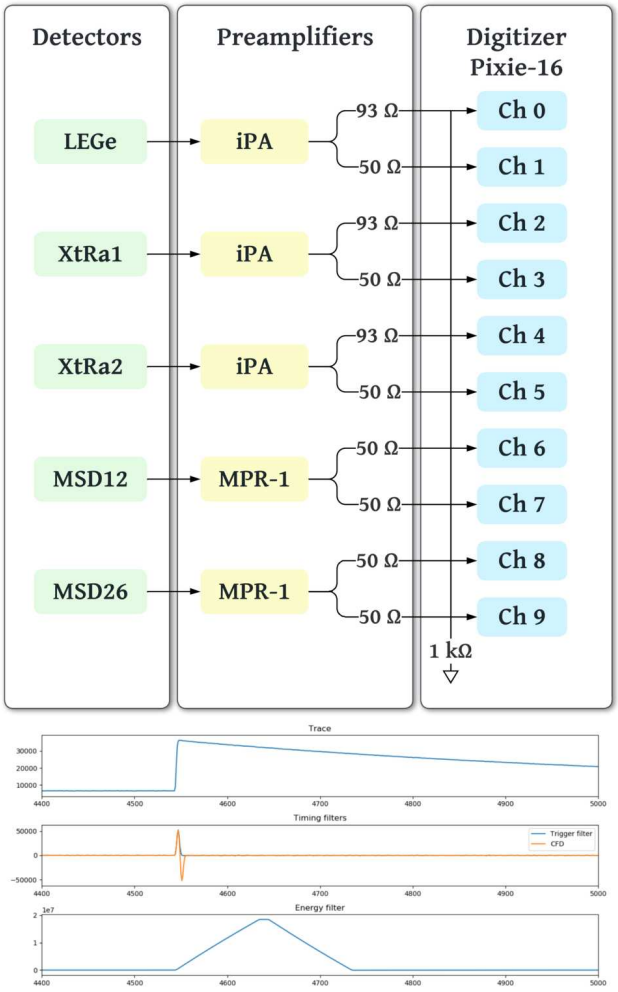

Figure 6: Schematic diagram of the electronics setup. The two arrows following each preamplifier indicate dual outputs with their impedance. The lower panel displays a generic preamplifier trace and the corresponding responses of the trigger filter, digital Constant Fraction Discriminator algorithm, and energy filter of DDAS.

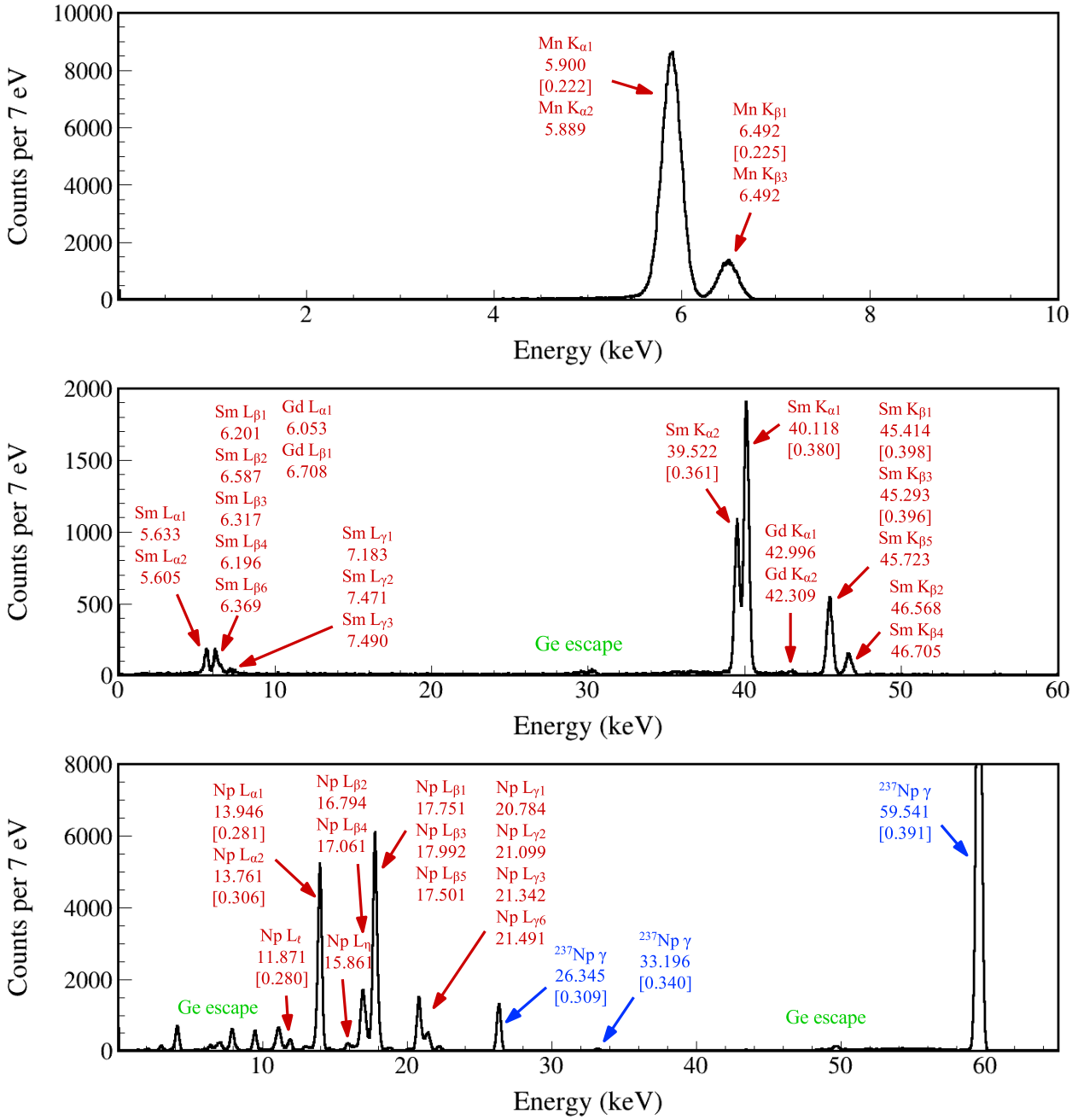

Figure 7: X-ray and/or γ-ray spectra measured by the LEGe detector using ^{55}Fe (top), ^{152}Eu (middle), and ^{241}Am (bottom) sources. All the X-ray energy values are adopted from Ref. [53] rounded to the nearest 0.01 keV. All the γ-ray energy values are adopted from Ref. [55] rounded to the nearest 0.01 keV. The FWHM values used to characterize the energy resolution of LEGe are indicated within brackets.

This phenomenon can potentially complicate the normalization of near-edge X rays. However, for our energies of interest in the range of 8-9 keV, K-shell absorption is no longer possible, and L-shell interactions dominate. In this case, incident gamma rays tend to penetrate somewhat deeper, and the energy of the fluorescent Ge L X rays is just 1.0−1.4 keV, resulting in a reduced probability of escape. By integrating the L X rays within the energy range of 5.4−8.1 keV in the ^{152}Eu spectrum in Fig. 7 and comparing it with the X-ray emission intensities [54], we estimate the corresponding detection efficiency to be 4.02(13)%.

4.2. γ-ray measurements

Figure 8 shows the γ-ray spectra measured by XtRa1 and XtRa2 using an ^{152}Eu point source. The achieved energy resolution aligns with the specifications provided by the manufacturer. Both XtRa detectors record an average of 300 room background gamma rays per second in our lab test environment. We first placed the source at the midpoint between two XtRa detectors that were facing each other, with a distance of 28 cm between them. We then placed the source at the center of the vacuum chamber. The two XtRa detectors were placed as close as possible to the two flanges (Fig. 4), with their entrance windows about 12 mm from the flange surface. XtRa1 Ge crystal has a slightly larger diameter than XtRa2. Both Ge crystals are 158.5 mm from the target center, covering 1.70% and 1.51% of the 4π solid angle, respectively. As can be seen from Fig. 8, both XtRa detectors exhibit good low-energy response to the ^{152}Eu X rays at 40 keV, while when the source is placed inside the chamber, the X rays are effectively blocked by the 3.175-mm thick stainless steel flanges.

We also tested XtRa with ^{60}Co and ^{137}Cs sources placed at the center of the chamber. The activity of the ^{152}Eu calibration source is quoted with 1.4% accuracy by the manufacturer [57]. The activities of the ^{60}Co and ^{137}Cs sources both have a 3% uncertainty. MSD12 was not in place during these tests due to its fragility. MSD26 and the Si detector holders attenuated the γ rays from the source to XtRa2 but had little effect on XtRa1. XtRa1 and XtRa2 have an absolute full-energy peak efficiency of 0.334(3)% and 0.286(3)% at 1 MeV, respectively, based on an exponential function that contains a polynomial of degree i with the natural log of the energy: $\varepsilon(E) = \exp\left[\sum_{i=1}^{6} p_i \ln(E)^i\right]$ fit on all the data points [58]. The error bars on the data points reflect the uncertainty of the γ-ray yields and the source activities, with an additional 2.5% to account for the true coincidence summing effect.

Our mechanical design allows the PXCT vacuum chamber to be integrated with larger γ-ray detector arrays, such as the DEcay Germanium Array initiator [59], to achieve an even higher γ-ray detection efficiency.

4.3. α-particle measurements

Figure 10 shows the α spectrum measured by MSD26 using an ^{241}Am source. Figure 11 shows the ΔE-E α spectrum measured by the telescope formed by MSD12 and MSD26. The α sum peak exhibits an energy resolution of 0.95%. In the ^{60}Ga experiment, the telescope will also be used to detect protons, which is anticipated to provide a higher resolution compared to that of α's. Using the ^{148}Gd and ^{241}Am sources, we calibrated MSD26 and then measured the residual energy of ^{241}Am α particles in MSD26 with MSD12 installed in front of it. This allowed us to accurately determine the effective thickness of MSD12 to be 11.65(8) μm. Taking into account the thickness of 350 nm of the 9.5P/7P window, it brought the total thickness to a value that is consistent with the nominal value of 12 μm given in the Micron datasheet.

4.4. Coincidence measurements

We placed an ^{241}Am source at the center of the chamber, 11.7 mm away from MSD12 and 10.5 mm away from the entrance window of LEGe. Figure 12 shows the α-γ coincidence spectrum between the MSD detector telescope and LEGe. The majority of low-energy photons emitted from ^{241}Am are blocked by the source substrate, leaving only the 59.54-keV γ ray in ^{237}Np and its escape peaks noticeable.

We placed an ^{152}Eu source at the center of the chamber. Figure 13 shows the XtRa1 γ spectra gated by the Sm K X rays measured by LEGe and gated by the electrons measured by MSD26, respectively. By applying the X-ray coincidence condition, both the room background γ rays and the β^--delayed γ rays from ^{152}Gd are substantially suppressed, and in turn, the electron coincidence condition suppresses the room background and EC-delayed γ ray lines from ^{152}Sm. Having electron/positron detection capability would help us to clean up the in-beam spectrum, thereby facilitating the identification of ^{60}Ga β^+-delayed γ rays during the experiment.

4.5. Timing performance

The timing performance of electronics was first tested using a Canberra Model 1407P Pulse Pair Generator [61]. The dual pulses were separately fed into two Pixie-16 channels. The FWHM resolution of the time-difference distribution is estimated to be 0.46 ns. Then, the primary pulse was split and fed to each test input of preamplifiers, and the resulting FWHM timing resolutions are 37.4 ns (MSD12), 4.4 ns (MSD26), 1.2 ns (XtRa1), 1.8 ns (XtRa2). The amplitude resolutions obtained from the pulse test are 0.13% (Pulser), 3.17% (MSD12), 0.84% (MSD26), 0.26% (XtRa1), and 0.24% (XtRa2), demonstrating the electronics noise level present in the system.

The timing performance of the detectors was studied using an ^{241}Am source placed inside the chamber and a ^{152}Eu source placed outside of the chamber. The sources were positioned in such a way that the α-γ coincidences could be measured by MSD and LEGe, and γ-γ coincidences could be measured by LEGe and XtRa. Fig. 14 shows the time distributions between all the coincidences without any energy constraints. Based on these measurements, an event-build window can be defined to capture all prompt coincidences and some chance continuum for background subtraction in offline analysis. Note that the asymmetric tail in both α-γ time difference distributions is

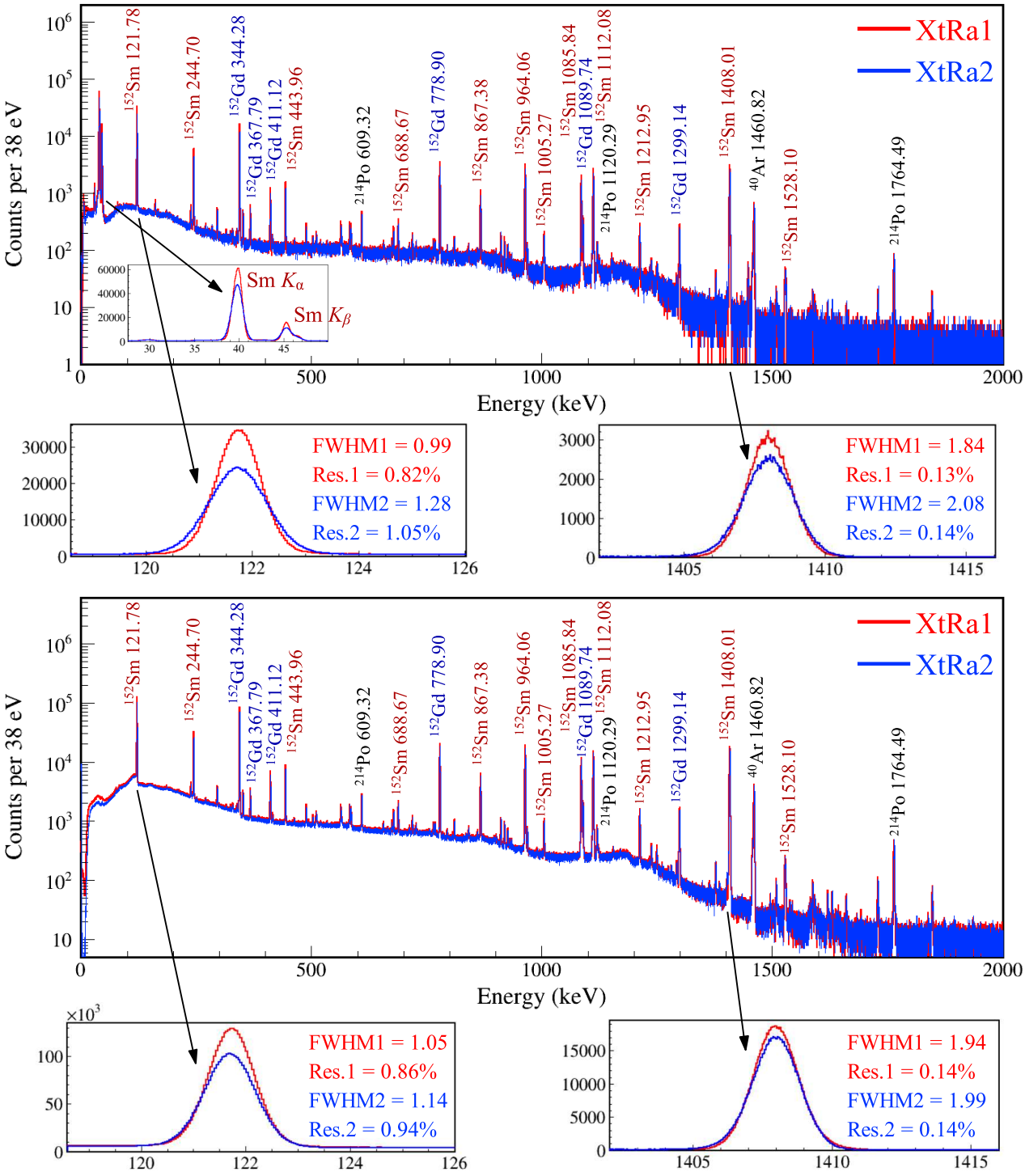

Figure 8: γ-ray spectra measured by XtRa1 (red) and XtRa2 (blue) using an ^{152}Eu source. Upper panel: the ^{152}Eu source is placed in the middle of the two XtRa facing each other. Lower panel: the ^{152}Eu source is placed at the center of the vacuum chamber, with the two XtRa detectors positioned according to the configuration shown in Fig. 4. All the γ-ray energy values are adopted from Ref. [56] rounded to the nearest 0.01 keV. The insets demonstrate the detector responses at 122 keV and 1408 keV.

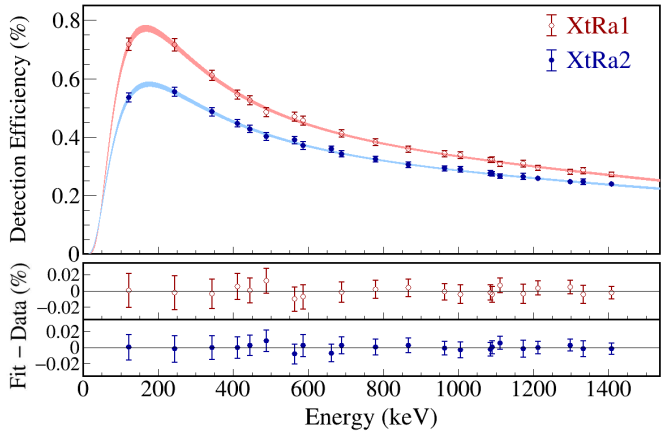

Figure 9: Absolute γ-ray detection efficiency of the two XtRa detectors obtained using ^{152}Eu, ^{137}Cs, and ^{60}Co sources placed at the center of the chamber. Please note that the ^{137}Cs data point at 662 keV is only applicable to XtRa2 due to the source geometry. The efficiency curves are represented by the 1σ uncertainty bands.

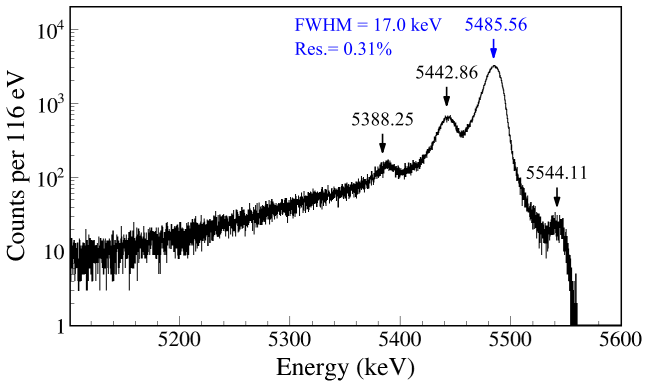

Figure 10: α spectrum measured by MSD26 using an ^{241}Am source. The α energy values are adopted from Ref. [60] rounded to the nearest 0.01 keV.

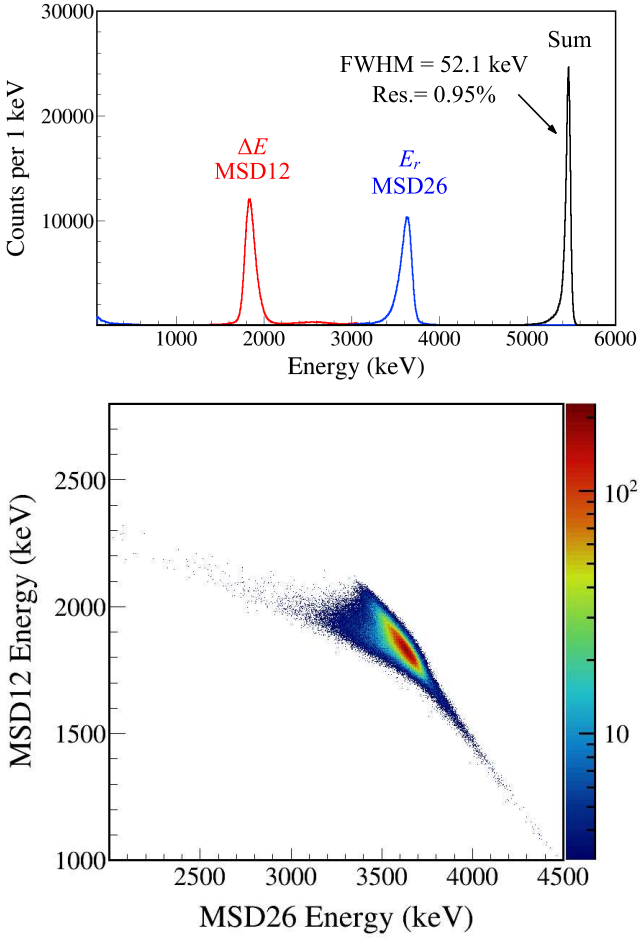

Figure 11: α spectrum measured by MSD12 and MSD26 using an ^{241}Am source. Upper: α-energy spectrum. Lower: ΔE-E 2D plot.

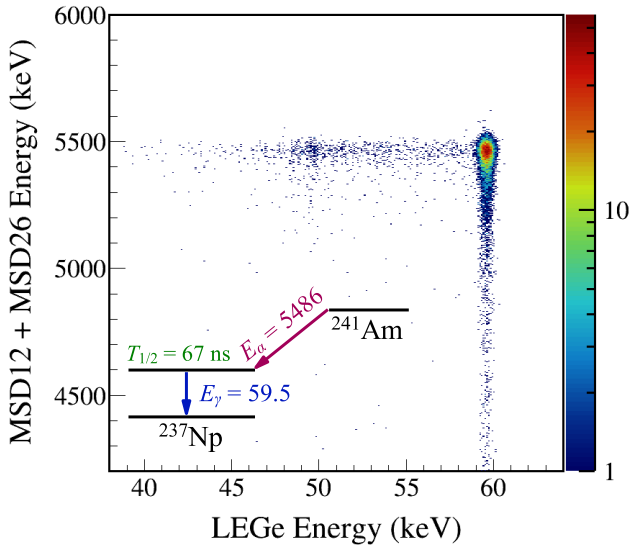

Figure 12: Coincidence spectrum between the MSD detector telescope and LEGe obtained using an ^{241}Am source placed at the center of the chamber. A simplified ^{241}Am decay scheme shows the dominant α-γ coincidence.

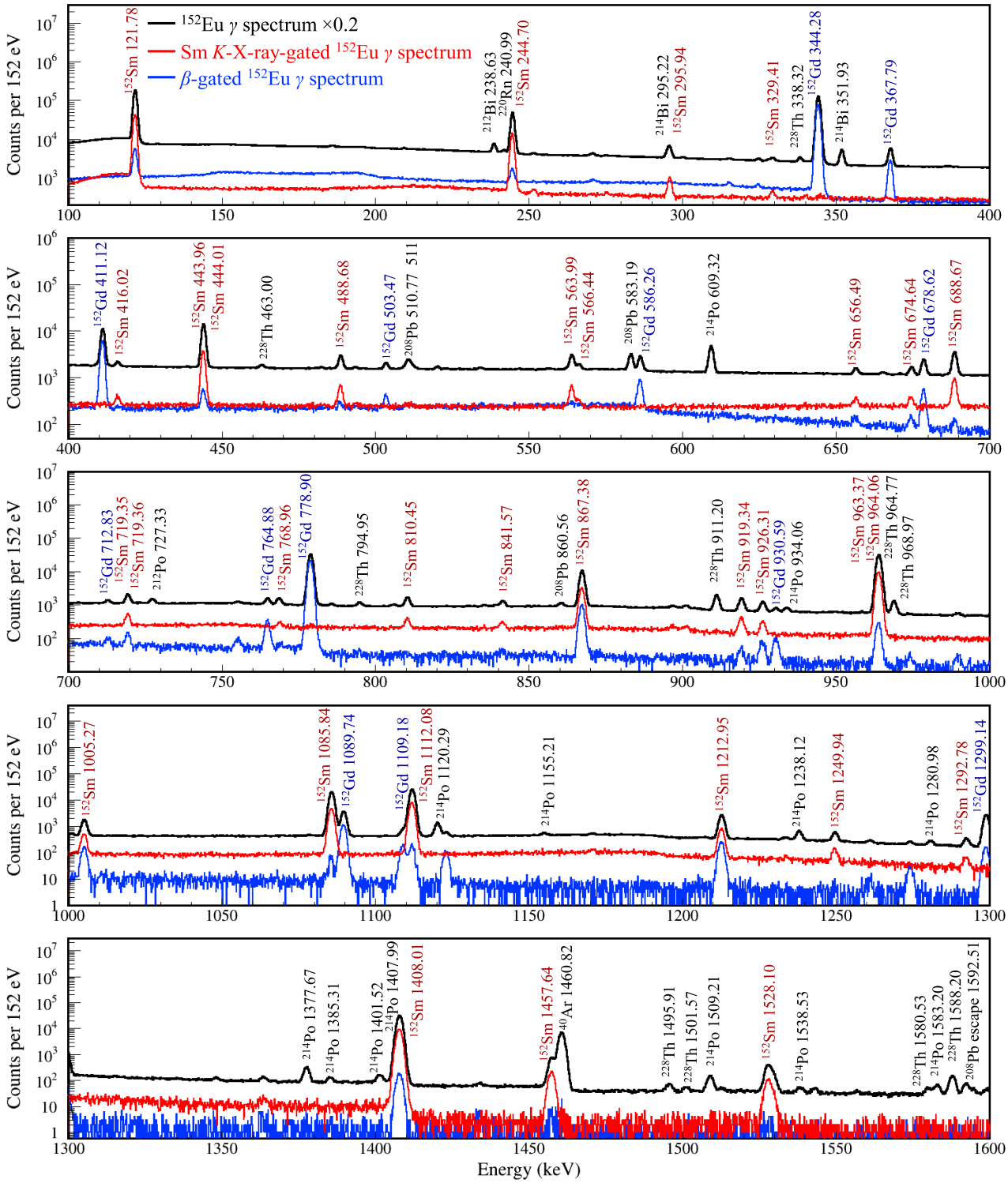

Figure 13: Black represents the raw γ-ray spectrum measured by XtRa1 using an ^{152}Eu source placed at the center of the chamber. Red represents the XtRa1 γ-ray spectrum gated by the Sm K_α and K_β X rays measured by LEGe. Blue represents the XtRa1 γ-ray spectrum gated by the electrons measured by MSD26. The raw spectrum is scaled down by a factor of 5 for better comparison.

attributed to the relatively long-lived 59.54-keV excited state of ^{237}Np. A dedicated analysis is provided in the next paragraph.

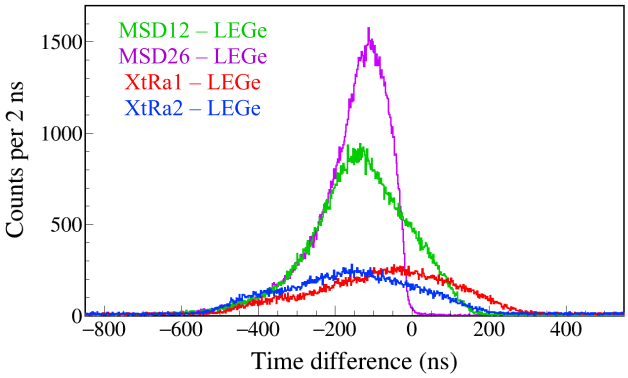

Figure 14: Coincidence time spectra between each detector obtained using an ^{241}Am source placed at the center of the chamber and a ^{152}Eu source placed outside of the chamber. The timestamps of the LEGe signals serve as the common reference for the other four detectors.

Figure 15 shows the α-γ time difference distribution constructed by the start timestamps from 5486-keV α measured by the two MSDs and the stop timestamps from the 59.54-keV γ ray deexciting the 59.54-keV state in ^{237}Np measured by LEGe. By fitting the distribution with a function composed of the total number of decays (N), the half-life of exponential decay (T), and a constant background (B), we obtained the half-life of the 59.54-keV excited state in ^{237}Np to be 68.08(9) ns (MSD12) and 68.01(7) ns (MSD26), respectively. The fit was conducted using the Bayesian method with the affine-invariant ensemble sampler for Markov chain Monte Carlo (MCMC) in the emcee package [62]. The MCMC was run with 100 walkers taking 10,000 steps, giving a total of 10^6 samples. The posterior results obtained from the MCMC sampling are demonstrated in Fig. 16. The half-life value and its 1σ uncertainties are determined by extracting the 16th, 50th, and 84th percentile values from the marginalized posterior distribution. The results obtained from both Si detectors are consistent with recent precision measurements of 67.86(9) ns [63] and 67.60(25) ns [64]. Two factors limit the time resolution that can be achieved with semiconductor detectors. Firstly, the charge collection process is inherently slow, typically taking several hundred nanoseconds. This timescale is much longer than the output from scintillators, making it hard to achieve the same level of timing performance. Secondly, the pulse rise shape from semiconductor detectors can vary significantly from event to event, resulting in a larger uncertainty in generating timestamps.

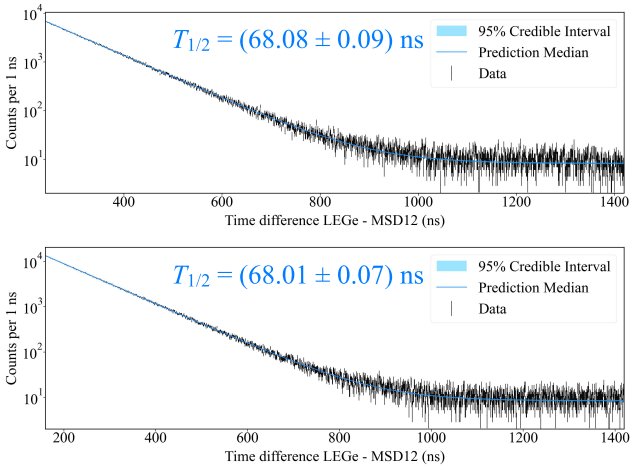

Figure 15: Time differences between the 59.54-keV γ-ray signals in LEGe and the 5486-keV α signals in the MSD silicon detector telescope.

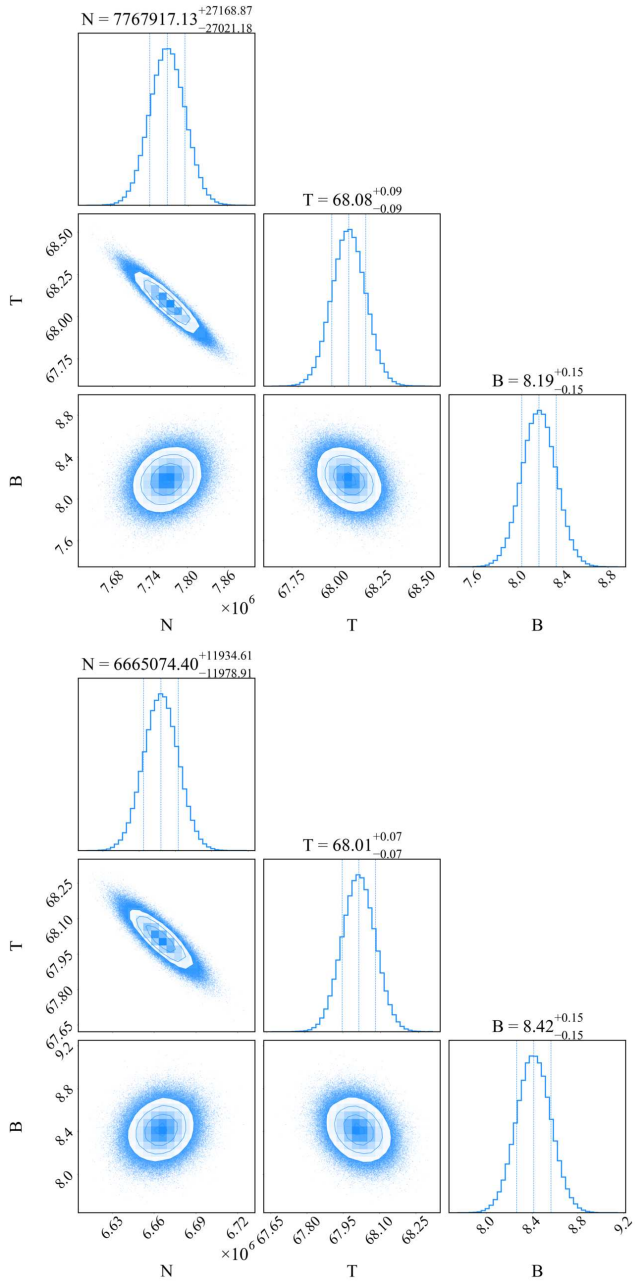

Figure 16: Posterior distributions of the decay fit parameters. Upper: MSD12. Lower: MSD26.

5. Summary

The technical details and the radioactive source test results of the PXCT detection system are reported. This setup has the ability to detect all the observables that are produced in the EC decay of ^{60}Ga. A complete dataset on ^{60}Zn resonances would help us to determine the competition between the ^{59}Cu$(p,\gamma)^{60}$Zn and ^{59}Cu$(p,\alpha)^{56}$Ni reactions, which is crucial for modeling of X-ray burst light curves and understanding the *rp*-process. Additionally, this setup may serve as a precise offline testing platform for harvested isotopes at FRIB.

6. Acknowledgements

This work was supported by the National Science Foundation (USA) under Grants No. PHY-1419765, No. PHY-1404442, No. PHY-1430152, No. PHY-1565546, No. PHY-1913554, and PHY-2209429, and No. the US Department of Energy, Office of Science, under Award No. DE-SC0016052, Contract No. DE-AC05-00OR22725, and the US Department of Energy National Nuclear Security Administration under Awards No. DE-NA0003221 and No. DE-NA0000979.

References

[1] J. C. Hardy, J. A. Macdonald, H. Schmeing, H. R. Andrews, J. S. Geiger, R. L. Graham, T. Faestermann, E. T. H. Clifford, and K. P. Jackson, Phys. Rev. Lett. **37**, 133 (1976).
[2] J. H. Scofield, *Atomic Inner-Shell Processes* (Academic Press: New York (NY), USA, 1975).
[3] W. Bambynek, B. Crasemann, R. W. Fink, H. U. Freund, H. Mark, C. D. Swift, R. E. Price, and P. Venugopala Rao, Rev. Mod. Phys. **44**, 716 (1972).
[4] J. Giovinazzo, Ph. Dessagne, and Ch. Miehé, Nucl. Phys. A **674**, 394 (2000).
[5] J. A. Macdonald, J. C. Hardy, H. Schmeing, T. Faestermann, H. R. Andrews, J. S. Geiger, R. L. Graham, and K. P. Jackson, Nucl. Phys. A **288**, 1 (1977).
[6] P. Asboe-Hansen, E. Hagberg, P. G. Hansen, J. C. Hardy, P. Hornshøj, B. Jonson, S. Mattsson, P. Tidemand-Petersson, Phys. Lett. B **77**, 363 (1978).
[7] P. Asboe-Hansen, E. Hagberg, P. G. Hansen, J. C. Hardy, B. Jonson, and S. Mattsson, Nucl. Phys. A **361**, 23 (1981).
[8] Z. Janas, L. Batist, R. Borcea, J. Döring, M. Gierlik, M. Karny, R. Kirchner, M. La Commara, S. Mandal, C. Mazzocchi, F. Moroz, S. Orlov, A. Płochocki, E. Roeckl, and J. Żylicz, Eur. Phys. J. A **24**, 205 (2005).
[9] Z. Janas, L. Batist, J. Döring, M. Gierlik, R. Kirchner, J. Kurcewicz, H. Mahmud, C. Mazzocchi, A. Płochocki, E. Roeckl, K. Schmidt, P. J. Woods, and J. Żylicz, Eur. Phys. J. A **23**, 401 (2005).
[10] J. José, *Stellar Explosions: Hydrodynamics and Nucleosynthesis* (CRC/Taylor and Francis: Boca Raton (FL), USA, 2016).
[11] H. Schatz and K. E. Rehm, Nucl. Phys. A **777**, 601 (2006).
[12] A. Parikh, J. José, G. Sala, and C. Iliadis, Prog. Part. Nucl. Phys. **69**, 225 (2013).
[13] R. H. Cyburt, A. M. Amthor, A. Heger, E. Johnson, L. Keek, Z. Meisel, H. Schatz, and K. Smith, Astrophys. J. **830**, 55 (2016).
[14] L. van Wormer, J. Görres, C. Iliadis, M. Wiescher, and F.-K. Thielemann, Astrophys. J. **432**, 326 (1994).
[15] C. E. Rolfs and W. S. Rodney, *Cauldrons in the Cosmos* (University of Chicago, Chicago, 1988).
[16] T. Rauscher, Phys. Rev. C **81**, 045807 (2010).

[17] D. Soltesz, M. A. A. Mamun, A. V. Voinov, Z. Meisel, B. A. Brown, C. R. Brune, S. M. Grimes, H. Hadizadeh, M. Hornish, T. N. Massey, J. E. O'Donnell, and W. E. Ormand, Phys. Rev. C **103**, 015802 (2021).

[18] M. Wang, W. J. Huang, F. G. Kondev, G. Audi, S. Naimi, Chin. Phys. C **45**, 030003 (2021).

[19] S. E. A. Orrigo, B. Rubio, W. Gelletly, P. Aguilera, A. Algora, A. I. Morales, J. Agramunt, D. S. Ahn, P. Ascher, B. Blank, C. Borcea, A. Boso, R. B. Cakirli, J. Chiba, G. de Angelis, G. de France, F. Diel, P. Doornenbal, Y. Fujita, N. Fukuda, E. Ganioğlu, M. Gerbaux, J. Giovinazzo, S. Go, T. Goigoux, S. Grévy, V. Guadilla, N. Inabe, G. G. Kiss, T. Kubo, S. Kubono, T. Kurtukian-Nieto, D. Lubos, C. Magron, F. Molina, A. Montaner-Pizá, D. Napoli, D. Nishimura, S. Nishimura, H. Oikawa, V. H. Phong, H. Sakurai, Y. Shimizu, C. Sidong, P.-A. Söderström, T. Sumikama, H. Suzuki, H. Takeda, Y. Takei, M. Tanaka, J. Wu, and S. Yagi, Phys. Rev. C **103**, 014324 (2021).

[20] S. F. Paul, J. Bergmann, J. D. Cardona, K. A. Dietrich, E. Dunling, Z. Hockenbery, C. Hornung, C. Izzo, A. Jacobs, A. Javaji, B. Kootte, Y. Lan, E. Leistenschneider, E. M. Lykiardopoulou, I. Mukul, T. Murböck, W. S. Porter, R. Silwal, M. B. Smith, J. Ringuette, T. Brunner, T. Dickel, I. Dillmann, G. Gwinner, M. MacCormick, M. P. Reiter, H. Schatz, N. A. Smirnova, J. Dilling, and A. A. Kwiatkowski, Phys. Rev. C **104**, 065803 (2021).

[21] E. Browne and J. K. Tuli, Nucl. Data Sheets **114**, 1849 (2013).

[22] C. Mazzocchi, Z. Janas, J. Döring, M. Axiotis, L. Batist, R. Borcea, D. Cano-Ott, E. Caurier, G. de Angelis, E. Farnea, A. Faßbender, A. Gadea, H. Grawe, A. Jungclaus, M. Kapica, R. Kirchner, J. Kurcewicz, S.M. Lenzi, T. Martínez, I. Mukha, E. Nácher, D. R. Napoli, E. Roeckl, B. Rubio, R. Schwengner, J. L. Tain, and C. A. Ur, Eur. Phys. J. A **12**, 269 (2001).

[23] M. J. López Jiménez, B. Blank, M. Chartier, S. Czajkowski, P. Dessagne, G. de France, J. Giovinazzo, D. Karamanis, M. Lewitowicz, V. Maslov, C. Miehé, P. H. Regan, M. Stanoiu, and M. Wiescher, Phys. Rev. C **66**, 025803 (2002).

[24] L. Kucuk, S. E. A. Orrigo, A. Montaner-Pizá, B. Rubio, Y. Fujita, W. Gelletly, B. Blank, Y. Oktem, T. Adachi, A. Algora, P. Ascher, R. B. Cakirli, G. de France, H. Fujita, E. Ganioğlu, J. Giovinazzo, S. Grévy, F. M. Marqués, F. Molina, F. de Oliveira Santos, L. Perrot, R. Raabe, P. C. Srivastava, G. Susoy, A. Tamii, J. C Thomas, Eur. Phys. J. A **53**, 134 (2017).

[25] B. A. Brown and W. D. M. Rae, Nucl. Data Sheets **120**, 115 (2014).

[26] M. Honma, T. Otsuka, B. A. Brown, and T. Mizusaki, Phys. Rev. C **69**, 034335 (2004).

[27] T. Rauscher and F. K. Thielemann, At. Data Nucl. Data Tables **75**, 1 (2000).

[28] C. Iliadis, *Nuclear Physics of Stars* (Wiley-VCH, Verlag, Wenheim, Germany, 2015).

[29] J. S. Randhawa, R. Kanungo, J. Refsgaard, P. Mohr, T. Ahn, M. Alcorta, C. Andreoiu, S. S. Bhattacharjee, B. Davids, G. Christian, A. A. Chen, R. Coleman, P. E. Garrett, G. F. Grinyer, E. Gyabeng Fuakye, G. Hackman, J. Hollett, R. Jain, K. Kapoor, R. Krücken, A. Laffoley, A. Lennarz, J. Liang, Z. Meisel, B. Nikhil, A. Psaltis, A. Radich, M. Rocchini, N. Saei, M. Saxena, M. Singh, C. Svensson, P. Subramaniam, A. Talebitaher, S. Upadhyayula, C. Waterfield, J. Williams, and M. Williams, Phys. Rev. C **104**, L042801 (2022).

[30] J. Wei, H. Ao, B. Arend, S. Beher, G. Bollen, N. Bultman, F. Casagrande, W. Chang, Y. Choi, S. Cogan, C. Compton, M. Cortesi, J. Curtin, K. Davidson, X. Du, K. Elliott, B. Ewert, A. Facco, A. Fila, K. Fukushima, V. Ganni, A. Ganshyn, J. Gao, T. Glasmacher, J. Guo, Y. Hao, W. Hartung, N. Hasan, M. Hausmann, K. Holland, H. C. Hseuh, M. Ikegami, D. Jager, S. Jones, N. Joseph, T. Kanemura, S.-H. Kim, P. Knudsen, B. Kortum, E. Kwan, T. Larter, R. E. Laxdal, M. Larmann, K. Laturkar, J. LeTourneau, Z.-Y. Li, S. Lidia, G. Machicoane, C. Magsig, P. Manwiller, F. Marti, T. Maruta, A. McCartney, E. Metzgar, S. Miller, Y. Momozaki, D. Morris, M. Mugerian, I. Nesterenko, C. Nguyen, W. O'Brien, K. Openlander, P. N. Ostroumov, M. Patil, A. S. Plastun, J. Popielarski, L. Popielarski, M. Portillo, J. Priller, X. Rao, M. Reaume, H. Ren, K. Saito, M. Smith, M. Steiner, A. Stolz, O. B. Tarasov, B. Tousignant, R. Walker, X. Wang, J. Wenstrom, G. West, K. Witgen, M. Wright, T. Xu, Y. Xu, Y. Yamazaki, T. Zhang, Q. Zhao, S. Zhao, K. Dixon, M. Wiseman, M. Kelly, K. Hosoyama, and S. Prestemon, Mod. Phys. Lett. A **37**, 2230006 (2022).

[31] M. Portillo, B.M. Sherrill, Y. Choi, M. Cortesi, K. Fukushima, M. Hausmann, E. Kwan, S. Lidia, P.N. Ostroumov, R. Ringle, M.K. Smith, M. Steiner, O.B. Tarasov, A.C.C. Villari, and T. Zhang, Nucl. Instrum. Methods Phys. Res. B **540**, 151 (2023).

[32] C.S. Sumithrarachchi, D.J. Morrissey, S. Schwarz, K. Lund, G. Bollen, R. Ringle, G. Savard, and A.C.C. Villari, Nucl. Instrum. Methods Phys. Res. B **463**, 305 (2020).

[33] K.R. Lund, G. Bollen, D. Lawton, D.J. Morrissey, J. Ottarson, R. Ringle, S. Schwarz, C.S. Sumithrarachchi, A.C.C. Villari, and J. Yurkon, Nucl. Instrum. Methods Phys. Res. B **463**, 378 (2020).

[34] A.C.C. Villari, G. Bollen, A. Henriques, A. Lapierre, S. Nash, R. Ringle, S. Schwarz, C.S. Sumithrarachchi, Nucl. Instrum. Methods Phys. Res. B **541**, 350 (2023).

[35] MIRCON MSD12 Circular Silicon Detector.

[36] MIRCON MSD26 Circular Silicon Detector.

[37] MIRION Low Energy Germanium Detector.

[38] MIRION Extended Range Coaxial Germanium Detector.

[39] MIRION Cryo-Pulse 5 PLUS Electrically Refrigerated Cryostat.

[40] MIRION Intelligent Preamplifier.

[41] ORTEC 660 Dual 5-kV Bias Supply.

[42] Mesytec MPR-1 Charge Integrating Preamplifier.

[43] Mesytec MHV-4 High Voltage Supply.

[44] Mesytec MNV-4 NIM Power Supply.

[45] XIA Pixie-16 Digitizer.

[46] K. Starosta, C. Vaman, D. Miller, P. Voss, D. Bazin, T. Glasmacher, H. Crawford, P. Mantica, H. Tan, W. Hennig, M. Walby, A. Fallu-Labruyere, J. Harris, D. Breus, P. Grudberg, W.K. Warburton, Nucl. Instrum. Methods Phys. Res. A **610**, 700 (2009).

[47] C.J. Prokop, S.N. Liddick, B.L. Abromeit, A.T. Chemey, N.R. Larson, S. Suchyta, J.R. Tompkins, Nucl. Instrum. Methods Phys. Res. A **741**, 163 (2014).

[48] XIA Pixie-16 Digitizer User Manual.

[49] H.Y. Wu, Z.H. Li, H. Tan, H. Hua, J. Li, W. Hennig, W.K. Warburton, D.W. Luo, X. Wang, X.Q. Li, S.Q. Zhang, C. Xu, Z.Q. Chen, C.G. Wu, Y. Jin, J. Lin, D.X. Jiang, Y.L. Ye, Nucl. Instrum. Methods Phys. Res. A **975**, 164200 (2020).

[50] BNC Model DB-2 NIM Random Pulse Generator.

[51] B. E. Glassman, D. Pérez-Loureiro, C. Wrede, J. Allen, D. W. Bardayan, M. B. Bennett, K. A. Chipps, M. Febbraro, M. Friedman, C. Fry, M. R. Hall, O. Hall, S. N. Liddick, P. O'Malley, W. -J. Ong, S. D. Pain, S. B. Schwartz, P. Shidling, H. Sims, L. J. Sun, P. Thompson, and H. Zhang, Phys. Rev. C **99**, 065801 (2019).

[52] L. J. Sun, M. Friedman, T. Budner, D. Pérez-Loureiro, E. Pollacco, C. Wrede, B. A. Brown, M. Cortesi, C. Fry, B. E. Glassman, J. Heideman, M. Janasik, A. Kruskie, A. Magilligan, M. Roosa, J. Stomps, J. Surbrook, and P. Tiwari, Phys. Rev. C **103**, 014322 (2021).

[53] Matt Newville, easyXAFS, Matteo Levantino, Christian Schlepuetz, Damian Günzing, Max Rakitin, Sang-Woo Kim, and kalvdans, xraypy/XrayDB: (4.5.1). Zenodo (2023).

[54] M.-M. Bé, V. Chisté, C. Dulieu, X. Mougeot, E. Browne, V. Chechev, N. Kuzmenko, F. Kondev, A. Luca, M. Galán, A.L. Nichols, A. Arinc, and X. Huang, Table of Radionuclides, Bureau International des Poids et Mesures (2004).

[55] M. Basunia, Nucl. Data Sheets **107**, 2323 (2006).

[56] M. J. Martin, Nucl. Data Sheets **114**, 1497 (2013).

[57] D. Weisshaar, D. Bazin, P.C. Bender, C.M. Campbell, F. Recchia, V. Bader, T. Baugher, J. Belarge, M.P. Carpenter, H.L. Crawford, M. Cromaz, B. Elman, P. Fallon, A. Forney, A. Gade, J. Harker, N. Kobayashi, C. Langer, T. Lauritsen, I.Y. Lee, A. Lemasson, B. Longfellow, E. Lunderberg, A.O. Macchiavelli, K. Miki, S. Momiyama, S. Noji, D.C. Radford, M. Scott, J. Sethi, S.R. Stroberg, C. Sullivan, R. Titus, A. Wiens, S. Williams, K. Wimmer, S. Zhu, Nucl. Instrum. Methods Phys. Res. A **847**, 187 (2017).

[58] M. B. Bennett, C. Wrede, S. N. Liddick, D. Pérez-Loureiro, D. W. Bardayan, B. A. Brown, A. A. Chen, K. A. Chipps, C. Fry, B. E. Glassman, C. Langer, N. R. Larson, E. I. McNeice, Z. Meisel, W. Ong, P. D. O'Malley, S. D. Pain, C. J. Prokop, H. Schatz, S. B. Schwartz, S. Suchyta, P. Thompson, M. Walters, and X. Xu, Phys. Rev. C **97**, 065803 (2018).

[59] FRIB Decay Station White Paper.

[60] M.-M. Bé, V. Chisté, C. Dulieu, X. Mougeot, E.

Browne, V. Chechev, N. Kuzmenko, F. Kondev, A. Luca, M. Galán, A.L. Nichols, A. Arinc, and X. Huang, Table of Radionuclides, Bureau International des Poids et Mesures (2010).
[61] Canberra Model 1407P Pulse Pair Generator.
[62] D. Foreman-Mackey, D. W. Hogg, D. Lang, and J. Goodman, Publ. Astron. Soc. Pac. **125**, 306 (2013).
[63] Marcell P. Takács, Karsten Kossert, Appl. Radiat. Isot. **176**, 109858 (2021).
[64] Chavdar Dutsov, Benoît Sabot, Philippe Cassette, Krasimir Mitev, Appl. Radiat. Isot. **176**, 109845 (2021).